Strong Inter-valley Electron-Phonon Coupling in Magic-Angle Twisted Bilayer Graphene

Cheng Chen[1]*, Kevin P. Nuckolls[2,3]*, Shuhan Ding[4], Wangqian Miao[5], Dillon Wong[2,3], Myungchul Oh[2,3], Ryan L. Lee[2,3], Shanmei He[1], Cheng Peng[1], Ding Pei[6], Yiwei Li[7], Shihao Zhang[6], Jianpeng Liu[6], Zhongkai Liu[6], Chris Jozwiak[8], Aaron Bostwick[8], Eli Rotenberg[8], Chu Li[9], Xu Han[9], Ding Pan[9], Xi Dai[9], Chaoxing Liu[10], B. Andrei Bernevig[3,11,12], Yao Wang[4], Ali Yazdani[2,3], Yulin Chen[1,6]

[1]*Department of Physics, University of Oxford, Oxford, OX1 3PU, United Kingdom*

[2]*Joseph Henry Laboratories, Jadwin Hall, Princeton University, Princeton, NJ, USA*

[3]*Department of Physics, Princeton University, Princeton, NJ, USA*

[4]*Department of Physics and Astronomy, Clemson University, Clemson, South Carolina 29631, USA*

[5]*Materials Department, University of California, Santa Barbara, California 93106-5050, USA*

[6]*School of Physical Science and Technology, ShanghaiTech University, Shanghai, 201210 P. R. China*

[7]*Institute for Advanced Studies (IAS), Wuhan University, Wuhan 430072, China*

[8]*Advanced Light Source, Lawrence Berkeley National Laboratory, Berkeley, CA 94720, USA*

[9]*Department of Physics, Hong Kong University of Science and Technology, Clear Water Bay, Hong Kong, China*

[10]*Department of Physics, the Pennsylvania State University, University Park, Pennsylvania 16802, USA*

[11]*Donostia International Physics Center, P. Manuel de Lardizabal 4, 20018 Donostia-San Sebastian, Spain*

[12]*IKERBASQUE, Basque Foundation for Science, Bilbao, Spain*

*These authors contributed equally to this work

The unusual properties of superconductivity in magic-angle twisted bilayer graphene (MATBG) have sparked enormous research interest[1-13]. However, despite the dedication of intensive experimental efforts and the proposal of several possible pairing mechanisms[14-22], the origin of its superconductivity remains elusive. Here, using angle-resolved photoemission spectroscopy with micrometer spatial resolution, we discover replicas of the flat bands in superconducting MATBG unaligned with its hexagonal boron nitride (hBN) substrate, which are absent in non-superconducting MATBG aligned with the hBN substrate. Crucially, the replicas are evenly spaced in energy, separated by 150 ± 15 meV, signalling the strong coupling of electrons in MATBG to a bosonic mode of this energy. By comparing our observations to simulations, the formation of replicas is attributed to the presence of strong inter-valley electron-phonon coupling to a K-point phonon mode. In total, the observation of these replica flat bands and the corresponding phonon mode in MATBG could provide important information for understanding the origin and the unusual properties of its superconducting phase.

Magic-angle twisted bilayer graphene (MATBG) has attracted extensive research interest as a versatile platform for the study of strongly correlated electronic phenomena[1-13], due to its distinct tunability. Many novel electronic states have been discovered in this low-density electron system, such as superconductivity, strongly correlated insulating states, pseudogap phases, topological phases and orbital magnetism[12,13]. Some of these phenomena are likely related to strong electronic Coulomb interactions, which can dominate over the kinetic energy in flat band systems[12,13]. However, the origin of the unusual superconducting state remains unresolved, despite several proposed pairing mechanisms derived from strong electronic correlations[14-17], electron-phonon interactions[18-20], spin fluctuations[21], and skyrmions[22].

In the past few decades, angle-resolved photoemission spectroscopy (ARPES) has served as an important tool for studying quantum materials due to its unique ability to directly visualize the electronic structure of materials in momentum space[23,24]. However, the small size ($\approx$ 1-10 μm) of two-dimensional material devices and the observed twist angle inhomogeneity in most MATBG devices[25] prohibit the application of conventional ARPES techniques due to its insufficient spatial resolution ($\approx$ 50-500 μm). Fortunately, recent advances in high-throughput X-ray optics[26] have enabled us to perform high-quality ARPES measurements with sub-μm spatial resolution (μ-ARPES), making it suitable for the study of the electronic structure of MATBG devices[27,28].

In this work, using μ-ARPES, we investigate and compare the electronic structures of superconducting and non-superconducting MATBG devices, tuned by the degree of alignment between MATBG and its underlying hexagonal boron nitride (hBN) substrate[11]. Remarkably, in the hBN-unaligned (superconducting) MATBG device, we observe an unusual set of replicas of the flat band at higher binding energies, where strong spectral intensity features are observed with energy and momentum characteristics that emulate those of the original flat band. These replicas are observed throughout the momentum range of the entire moiré Brillouin zone (BZ) and are evenly separated in energy by 150 ± 15 meV. In contrast, under the same experimental

conditions, no replicas of the flat band are evidenced in the hBN-aligned (non-superconducting) MATBG device. These experimental observations naturally suggest a correlation between the microscopic mechanisms responsible for replicas of the flat band and for superconductivity in MATBG. The observation of replicated bands at higher binding energies in the single-particle ARPES spectrum goes beyond the predictions of non-interacting band theories and often indicates a strongly correlated origin[29-31]. Combining theoretical model analysis and nonperturbative many-body simulations[19,32], we found that in MATBG, the strong coupling of flat band electrons to a transverse optical phonon mode at the graphene K point can explain the observed replicas through an inter-valley scattering process (details and discussion will be presented below and in Ref. 32). Overall, our results provide insight into the interplay between flat band electrons and the bosonic degrees of freedom of MATBG, which may further reveal its complex electronic settings from which superconductivity emerges.

For this study, we perform ARPES measurements on hBN-unaligned and hBN-aligned MATBG samples used in a previous scanning tunnelling microscopy / spectroscopy (STM / STS) study[11], where the twist angle, the spectroscopic properties, and the presence or absence of superconductivity have been confirmed. A schematic of the μ-ARPES measurement is shown in Fig. 1a (the Au pad connected to the MATBG sample is grounded to ensure no charge accumulation on the sample during measurements). The geometry of the hBN-unaligned and hBN-aligned MATBG samples (optical images) are shown in Fig. 1b(i) and Fig. 1c(i), respectively. Notably, with the capability of μ-ARPES to directly resolve the MATBG band structure, photoemission intensity maps of each sample can easily distinguish the MATBG regions from the hBN substrate (Fig. 1b(ii)) or single-layer graphene regions (Fig. 1c(ii)).

Although these MATBG devices were observed in STM topographic images to be of nearly the same twist angle (1.06° and 1.08°, close to the twist angle where superconductivity T_c is maximized in transport measurements[1,33]), only the hBN-unaligned device was found superconducting while no evidence of superconductivity or the pseudogap regime was observed in the hBN-aligned device[11] (See Supplementary Information (SI), Section I). This is possibly

due to the effect of different moiré potentials, caused by different forms and degrees of coupling between MATBG and its hBN substrate, as can be seen in Fig. 1b(iii) and Fig. 1c(iii). In the unaligned sample (Fig. 1b(iii)), the hBN substrate introduces a high-frequency spatial background to the intrinsic MATBG moiré potential (Fig. 1d) due to the large angle (8°) mismatch between the hBN and MATBG, which does not significantly alter the electronic structure of MATBG. In contrast, in the aligned sample, the moiré periodicity (~13nm) introduced by the hBN substrate is comparable to that of intrinsic MATBG (13.8nm) – see Fig. 1b(iii) – due to its small twist angle (0.5°±0.1°) with respect to the bottom graphene layer. In this device, the graphene-hBN moiré potential and induced C_2-symmetry-breaking can strongly interfere with the electronic structure of pristine MATBG, as we will discuss later.

In Fig. 2, we show ARPES data of the hBN-unaligned (superconducting) MATBG sample. All measurements were carried out in the vicinity of the K points of the individual graphene layers throughout a few moiré BZs (Fig. 2a). A three-dimensional (3D) band structure map is presented in Fig. 2b and six representative band dispersion spectra across the moiré BZs are presented in Fig. 2c. Near the Fermi level (E_F), we observe features of the flat band of MATBG, which extend throughout the entire moiré BZ and are well-described by single-particle calculations, as previously reported[27,28]. Remarkably, however, we observe previously unresolved replicas of this flat band appearing at higher binding energies, with similar bandwidth, momentum range, and spectral distribution as the original flat band (Fig. 2c). These features are best resolved in a series of ARPES dispersion spectra cutting across the moiré BZ at different momentum locations (see corresponding labels for 'cut 1' ~ 'cut 6' in Fig. 2a, b). The replicas are distinct from the dispersive Dirac bands of the two graphene layers and the flat band near E_F by their binding energies. Such replica features cannot be explained by typical band hybridizations because they are evenly separated in energy by 150 ± 15meV, and are not observed to be localized to high-symmetry momenta in the moiré BZ. We observe the intensities of these replica features to decrease rapidly at higher binding energies, as shown in both the dispersion plots in Fig. 2c and the spectra intensity analysis in Fig. 2d (see also Section II of

SI). To summarize our observations, the bare Dirac bands of the two graphene layers, the flat band, and the replica flat band features are schematically depicted in Fig. 2e.

We perform similar measurements of the electronic structure of the hBN-aligned (non-superconducting) MATBG sample under identical measurement conditions (Fig. 3). In contrast, we observe no signatures of the replica features in this sample, despite the twist angle and strain of this device being nearly identical to those of the hBN-unaligned device. Instead, the band structure of this sample shows typical signatures of band hybridization between the Dirac bands of two graphene layers, which is further modified by the commensurate MATBG/hBN moiré potential (Fig. 1b(iii)). Further discussion of the band dispersions of the hBN-aligned MATBG sample and its comparison to the unaligned sample can be found in Section III of SI.

The observation of replica bands at higher binding energies in single-particle ARPES spectra usually indicates the existence of strong electron-boson coupling in the system[29-31]. Here in MATBG, the coincident appearance of the replica flat bands and superconductivity (only in the hBN-unaligned sample) further indicates that they may have connected underlying mechanisms. This connection strongly parallels the observation of shake-off replica bands in FeSe/SrTiO$_3$[29,34,35], which likely arise from the strong coupling of electrons in monolayer FeSe to an optical phonon mode in SrTiO$_3$. This strong electron-phonon coupling (EPC) was proposed to be responsible for the much enhanced superconducting transition temperature in this composite system as compared to FeSe alone[29,34,35]. Although there are many bosonic modes in MATBG, few are consistent with our observations. For example, collective spin fluctuations (which couple to electrons to form magnetic polarons) can be excluded by our measurement because the energy spacing of the resulting replica bands would be uneven[36]. Plasmons (which couple to electrons to form plasmarons) are also unlikely candidates because the energy separation of the resulting replicas would be much smaller than 150 meV[37,38] due to the low carrier density in intrinsic MATBG/hBN[1]. Phonons (which couple to electrons to form polarons), however, can have mode energies around 150 meV, which matches the energy spacing of the observed replicas, and therefore are considered as the most likely origin[29-31,34,35].

As the electronic kinetic energy of the flat bands in MATBG ($\approx$ 10-15 meV) is

negligible compared with the large mode energy ($\approx$ 150meV), we first examine the intrinsic phonon spectra of graphene without considering the renormalization caused by polaronic dressing. To generate replica features in both moiré BZs, the contributing phonon modes should reside around the Γ or K (K') point in the original graphene BZ to couple with the corresponding intra- or inter-valley electron-hole processes, respectively. In Fig. 4a, three phonon branches with energies around 150 meV near the K point are highlighted (by green, red and blue colors) as candidates that can potentially mediate inter-valley EPC. Among the three modes, the in-plane transverse optical (iTO) mode has the highest EPC strength (see Fig. 4b), dominant over the other two (iLO, iLA) relevant modes according to our frozen-phonon calculations (see Section IV, V of SI for details; the lattice distortion induced by iTO modes is illustrated in Fig. 4c). This significant difference stems from the symmetry of flat-band wavefunctions and two-center approximation[32], consistent with previous studies[39,40].

The iTO phonon mode scatters flat-band electrons between the moiré BZs at K and K' points (Fig. 4d), leading to a series of shake-off replica bands similar to those of forward-scattering phonons in each moiré BZ. Using the frozen-phonon simulations and flat-band tight-binding models, we reproduce the replica features in ARPES spectra (shown in Fig. 4e, details can be found in the Method and Section VI of SI), whose energy separation is determined by the phonon energy due to its dominance over the ~15 meV electronic bandwidth[29-31]. The relative intensity of the first two replicas is comparable to our experiment result shown in Fig. 2, without fitting any parameters from the latter.

We now discuss how this experimentally identified EPC may further contribute to electronic pairing in MATBG. Our raw estimation indicates that MATBG lies in the strong-coupling regime (See Section V of SI), consistent with the observation of a pseudogap above T_c[11]. We stress that the contribution of phonons does not necessarily lead to conventional s-wave superconductivity, given the topological nature of multiple flat bands[32]. It has been found that inter-valley EPC can also mediate d-wave pairing in the intra-Chern-band channel[19,32], which allows for time-reversal breaking chiral d-wave pairing or gapless nematic d-wave pairing[41], the latter being consistent with previous STS observations of a nodal tunneling gap[11].

In addition, our electron-phonon calculations exclude contributions from the large Coulomb repulsion between electrons, which cannot be sufficiently screened in the flat-band systems. The coexistence of both strong EPC and Coulomb repulsions is expected to further complicate the pairing symmetry in MATBG and may cooperate in stabilizing superconductivity, as recently discussed in cuprates[42-44]. At low temperatures, these pairing properties would be reflected by electronic properties within the energy window of each replica, which cannot be accessed by current μ-ARPES techniques due to its temperature (≈ 20 K) and resolution limitation (≈ 20 meV). However, we stress that the nature of electronic many-body states does not affect the quantification of polaronic replica features at the energy scale of 150 meV (see the derivations in the Sec. VI of SI) and are thus unlikely to significantly affect the interpretation presented above.

Our results motivate the importance of inter-valley phonon modes in superconducting MATBG, which act to dress the electronic states of the flat bands in ways that broadly parallel those found in iron-based high-T_c superconductors. Questions remain on the influence of hBN alignment upon MATBG, which significantly alters its electronic structure and leads to distinctive emergent phenomena[5,6,11,13]. One possible explanation is that the additional moiré potential modulation results in effective charge impurities in MATBG, which may suppress its superconductivity (as well as the replicas of the flat band) similar to that in cuprate superconductors[45-47]. Going forward, we expect future experimental efforts to further clarify the connection between the microscopic mechanisms driving replica flat bands to those driving superconductivity in twisted graphene systems. For instance, similar replica flat bands may appear in superconducting magic-angle twisted trilayer graphene[48], while they may be absent in non-superconducting twisted monolayer-bilayer graphene[49]. Furthermore, we expect that the distinct capabilities of μ-ARPES (and more advanced Nano-ARPES) will be broadly utilized in the study of strong correlation effects in moiré systems.

Methods:

Sample fabrication

The hBN-unaligned and hBN-aligned MATBG devices are Device B and Device C from Ref.

11 (the full description of the fabrication procedure can be found in this reference). Briefly, devices were fabricated using a 'tear-and-stack' method[50] in which a single graphene sheet is torn in half by van der Waals interaction with hBN. The two halves are rotated relative to each other and stacked to form MATBG. Graphene, graphite (in the aligned device) and hBN are picked up with polyvinyl alcohol. Then, to flip the heterostructure upside down, the heterostructure is pressed against an intermediate structure consisting of polymethyl methacrylate/transparent tape/Sylgard 184, and the polyvinyl alcohol is dissolved via water injection. The heterostructure is then transferred to a SiO_2/Si chip with pre-patterned Ti/Au electrodes. Residual polymer is dissolved in dichloromethane, water, acetone, and isopropyl alcohol. These chips have been annealed in ultra-high vacuum at 170 °C overnight and 400 °C for 2 h for previous STM measurements[11].

Spatial- and Angle-resolved photoemission spectroscopy (μ-ARPES)

Synchrotron-based μ-ARPES measurements were performed at Beamline 7.0.2 (MAESTRO) of Advanced Light Source (ALS), USA. The samples were annealed in ultra-high vacuum at 300 °C for 3h and measured under ultra-high vacuum below 3×10^{-11} Torr. The photon energy of the incident beam is 95eV and the measurement is performed at room temperature. Data was collected using R4000 analyser upgraded with deflectors. The incoming photon beam is focused down to 2um spot size by using a capillary mirror[26]. The total energy and angle resolutions were 20 meV and 0.1°, respectively.

Model calculation

1. Estimation of Electron-Phonon Coupling

We adopt the following non-interacting-electron tight-binding Hamiltonian to calculate the electronic structure and EPC of MATBG,

$$H = - \sum_{Ii\alpha, Jj\beta} t(\boldsymbol{R}_{Ii\alpha} - \boldsymbol{R}_{Jj\beta}) c^\dagger_{Ii\alpha} c_{Jj\beta}$$

where $c^\dagger_{Ii\alpha}$, $c_{Jj\beta}$ are creation and annihilation operators for the p_z orbital of $i\alpha$ carbon atom in the I-th moiré superlattice (α, β are joint indices for sublattices and layers). The impact of atomic coordinates on the hopping parameter t is approximated by Slater-Koster formula, whose dependence on atomic coordinates sets the stage for the EPC estimation. The Slater-Koster parameters are specified in the SI.

To evaluate the coupling in the mini-BZ, we further project the coupling matrix using Truncated Atomic Plane Wave (TAPW) method[40,51]. Thus, a moiré phonon near the Γ_M point can be approximated by iTO/iLA/iLO phonons at graphene K/K' points. (see SI for details). We set the moiré phonon energy $\omega_0 = 150 meV$, the mass of carbon atoms $m_c =$

$2.0 \times 10^{-26} kg$, and the characteristic phonon length $l_p = \sqrt{\hbar/(2m_c\omega_0)} = 34.0 \, m\text{Å}$. The TAPW electrons and projected EPC constitute the model Hamiltonian for the TBG system

$$H = -\sum_{\bar{k}\sigma} c^{(\text{TAPW})\dagger}_{\bar{k}\sigma} h_{\bar{k}} c^{(\text{TAPW})}_{\bar{k}\sigma} - \frac{1}{\sqrt{N_m}} \sum_{\bar{k}\sigma\bar{q}\nu} c^{(\text{TAPW})\dagger}_{\bar{k}+\bar{q}\sigma} M_{\bar{q}\nu} c^{(\text{TAPW})}_{\bar{k}\sigma} \left(a_{\bar{q}\nu} + a^{\dagger}_{-\bar{q}\nu}\right) + \sum_{\bar{q}\nu} \omega_0 a^{\dagger}_{\bar{q}\nu} a_{\bar{q}\nu}$$

where $c^{(\text{TAPW})}_{\bar{k}\sigma}$ is the column vector of electron annihilation operators with moiré momentum $\bar{k}$ and spin σ in the TAPW basis and $h_{\bar{k}}$ is the electronic hopping matrix for a specific moiré momentum $\bar{k}$. The size of its moiré mini-BZ is denoted as N_m to distinguish from the system size N. For folded phonon branches, $a_{\bar{q}\nu}$ is the annihilation operator with moiré momentum $\bar{q}$ and ν labels the index of branches. The average distance between phonons and electrons is small compared to the moiré length scale. Therefore, the coupling matrix $M_{\bar{q}\nu}$ can be estimated by the momentum-independent M_0, which can be evaluated by the frozen-phonon calculations.

As the experimentally relevant electrons lie in low-energy flat bands, we further project the TAPW orbitals onto the four flat-band orbitals, which can be expressed as the projection operator $c^{(\text{flat})}_{\bar{k}\sigma} = P^{\dagger}_{\bar{k}} c^{(\text{TAPW})}_{\bar{k}\sigma}$. In the projected Hamiltonian, the EPC matrix becomes a 4×4-dimensional $\widetilde{M}_{\bar{k}}(\bar{q}) = P^{\dagger}_{\bar{k}+\bar{q}} M_0 P_{\bar{k}}$. Note that the projected coupling matrix becomes dependent on both the phonon momentum $\bar{q}$ and the electronic momentum $\bar{k}$. However, based on its numerical distribution, we find that $\widetilde{M}_{\bar{k}}(\bar{q})$ can be approximated by $U_{\bar{k}+\bar{q}} g_{\bar{q}} \eta U^{\dagger}_{\bar{k}}$, where η is a constant diagonal matrix, as shown in SI. Thus, the projected Hamiltonian becomes

$$H_{\text{flat−band}} = \sum_{\bar{k}\sigma} c^{\dagger}_{\bar{k}\sigma} U^{\dagger}_{\bar{k}} \varepsilon_{\bar{k}} U_{\bar{k}} c_{\bar{k}\sigma} - \frac{1}{\sqrt{N_m}} \sum_{\bar{k}\sigma\bar{q}\nu} g_{\bar{q}} c^{\dagger}_{\bar{k}+\bar{q}\sigma} \eta c_{\bar{k}\sigma} \left(a_{\bar{q}\nu} + a^{\dagger}_{-\bar{q}\nu}\right) + \sum_{\bar{q}\nu} \omega_0 a^{\dagger}_{\bar{q}\nu} a_{\bar{q}\nu}$$

where $c_{\bar{k}\sigma} = U^{\dagger}_{\bar{k}} c^{(\text{flat})}_{\bar{k}\sigma}$ and the diagonal matrix $\varepsilon_{\bar{k}}$ represents the energy of the flat bands.

2. ARPES Spectral Simulation

The strong EPC for the flat-band electrons leads to nonperturbative polaronic dressing effects. We consider the Lang-Firsov transformation for the coupled Hamiltonian

$$U_{\text{LF}} = e^{-\frac{1}{\sqrt{N_m}\omega_0} \sum_{\bar{R}\sigma\bar{q}\nu} e^{-i\bar{R}\cdot\bar{q}} g_{\bar{q}} c^{\dagger}_{\bar{R}\sigma} \eta c_{\bar{R}\sigma} \left(a_{\bar{q}\nu} - a^{\dagger}_{-\bar{q}\nu}\right)},$$

where $c_{\bar{R}\sigma}$ is the real-space annihilation operator of electron. Due to the separation of energy scales for electrons and phonons, we can employ the polaron ansatz for the ground-state wavefunction $|\Psi_G\rangle = U^{\dagger}_{\text{LF}} |\psi_e\rangle \otimes |\psi_{\text{ph}}\rangle$. Moreover, since both the transformed coupling strength $g_{\bar{q}}$ and temperature are much less than the phonon energy $\omega_0 = 150\text{meV}$, we further assume that the $|\psi_{\text{ph}}\rangle$ can be approximated by a vacuum state $|0_{\text{ph}}\rangle$. Thus, the electronic part $|\psi_e\rangle$ is determined by an effective Hamiltonian

$$\langle 0_{\text{ph}} | U_{\text{LF}} H U^{\dagger}_{\text{LF}} | 0_{\text{ph}} \rangle$$

$$= \sum_{\overline{R}\overline{R}'\sigma} c^\dagger_{\overline{R}\sigma} \langle 0_{\text{ph}}|h^*_{\overline{R}\overline{R}'}|0_{\text{ph}}\rangle c_{\overline{R}'\sigma} - \sum_{\overline{R}\overline{R}'\sigma\sigma'\overline{q}} \frac{N_v |g_{\overline{q}}|^2}{N_m\omega_0} e^{i(\overline{R}'-\overline{R})\cdot\overline{q}} \left(c^\dagger_{\overline{R}\sigma}\eta c_{\overline{R}\sigma}\right) \left(c^\dagger_{\overline{R}'\sigma'}\eta c_{\overline{R}'\sigma'}\right).$$

The $h^*_{\overline{R}\overline{R}'}$ is the phonon-dressed electronic hopping matrix, whose specific form is shown in SI. The ground state of the above equation determines the $|\psi_e\rangle$ in $|\Psi_G\rangle$ and electron properties (e.g. superconductivity), which are not studied in this paper.

The photoemission spectrum also involves excited states (denoted as $|\Phi\rangle$)

$$A(\overline{k},\omega) = \text{Im}\left\{ \frac{1}{N_m} \sum_{\overline{R}\overline{R}'} e^{-i(\overline{R}-\overline{R}')\cdot\overline{k}} \sum_{\sigma\alpha,\Phi} \langle \Psi_G|c^\dagger_{\overline{R}\sigma\alpha}|\Phi\rangle\langle \Phi|c_{\overline{R}'\sigma\alpha}|\Psi_G\rangle \frac{1}{\omega - i\Gamma + E_\Phi - E_G} \right\},$$

where Γ is the Lorentzian broadening. With the aforementioned ground-state ansatz, the amplitude can be expressed in the polaronic basis

$$\langle \Phi|c_{\overline{R}\sigma\alpha}|\Psi_G\rangle = \langle \psi_{\text{ph}}\{m_{\overline{q}v}\}|\otimes\langle \psi_e^{N_e-1}|U_{\text{LF}} c_{\overline{R}\sigma\alpha} U^\dagger_{\text{LF}}|\psi_e^{N_e}\rangle\otimes|0_{\text{ph}}\rangle$$

Thus, the intensity of the M-th replica peak is explicitly determined as

$$\frac{1}{M!}\exp\left(-\sum_{\overline{q}} \frac{N_v|g_{\overline{q}}|^2}{N_m\omega_0^2}\right)\left(\sum_{\overline{q}} \frac{N_v|g_{\overline{q}}|^2}{N_m\omega_0^2} e^{i\overline{R}\cdot\overline{q}}\right)^M.$$

It follows a Poisson distribution with the factor $\sum_{\overline{q}} \frac{N_v|g_{\overline{q}}|^2}{N_m\omega_0^2} \approx 0.11$, according to the frozen-phonon simulations. Focusing on the relative intensity of replica features and ignoring the interacting nature of electrons inside each replica, we produce the spectral simulation in Fig.4e.

REFERENCES

1   Cao, Y. *et al.* Unconventional superconductivity in magic-angle graphene superlattices. *Nature* **556**, 43-50, doi:10.1038/nature26160 (2018).

2   Cao, Y. *et al.* Correlated insulator behaviour at half-filling in magic-angle graphene superlattices. *Nature* **556**, 80-84, doi:10.1038/nature26154 (2018).

3   Lu, X. *et al.* Superconductors, orbital magnets and correlated states in magic-angle bilayer graphene. *Nature* **574**, 653-657, doi:10.1038/s41586-019-1695-0 (2019).

4   Yankowitz, M. *et al.* Tuning superconductivity in twistedbilayer graphene. *Science* **363**, 1059-1064 (2019).

5   Serlin, M. *et al.* Intrinsic quantized anomalous Hall effect in a moiré heterostructure. *Science* **367**, 900-903 (2020).

6   Sharpe, A. L. *et al.* Emergent ferromagnetism near three-quarters filling in twisted bilayer graphene. *Science* **365**, 605-608 (2019).

7   Kerelsky, A. *et al.* Maximized electron interactions at the magic angle in twisted bilayer graphene. *Nature* **572**, 95-100, doi:10.1038/s41586-019-1431-9 (2019).

8   Xie, Y. *et al.* Spectroscopic signatures of many-body correlations in magic-angle twisted bilayer graphene. *Nature* **572**, 101-105, doi:10.1038/s41586-019-1422-x (2019).

9   Nuckolls, K. P. *et al.* Strongly correlated Chern insulators in magic-angle twisted bilayer graphene. *Nature* **588**, 610-615, doi:10.1038/s41586-020-3028-8 (2020).

10   Wong, D. *et al.* Cascade of electronic transitions in magic-angle twisted bilayer

graphene. *Nature* **582**, 198-202, doi:10.1038/s41586-020-2339-0 (2020).

11   Oh, M. *et al.* Evidence for unconventional superconductivity in twisted bilayer graphene. *Nature* **600**, 240-245, doi:10.1038/s41586-021-04121-x (2021).

12   Andrei, E. Y. & MacDonald, A. H. Graphene bilayers with a twist. *Nat. Mater.* **19**, 1265-1275, doi:10.1038/s41563-020-00840-0 (2020).

13   Balents, L., Dean, C. R., Efetov, D. K. & Young, A. F. Superconductivity and strong correlations in moiré flat bands. *Nat. Phys.* **16**, 725-733, doi:10.1038/s41567-020-0906-9 (2020).

14   Dodaro, J. F., Kivelson, S. A., Schattner, Y., Sun, X. Q. & Wang, C. Phases of a phenomenological model of twisted bilayer graphene. *Phys. Rev. B* **98**, doi:10.1103/PhysRevB.98.075154 (2018).

15   Xu, C. & Balents, L. Topological Superconductivity in Twisted Multilayer Graphene. *Phys. Rev. Lett.* **121**, 087001, doi:10.1103/PhysRevLett.121.087001 (2018).

16   Guo, H., Zhu, X., Feng, S. & Scalettar, R. T. Pairing symmetry of interacting fermions on a twisted bilayer graphene superlattice. *Phys. Rev. B* **97**, doi:10.1103/PhysRevB.97.235453 (2018).

17   Guinea, F. & Walet, N. R. Electrostatic effects, band distortions, and superconductivity in twisted graphene bilayers. *Proc. Natl. Acad. Sci. USA* **115**, 13174-13179, doi:10.1073/pnas.1810947115 (2018).

18   Lian, B., Wang, Z. & Bernevig, B. A. Twisted Bilayer Graphene: A Phonon-Driven Superconductor. *Phys. Rev. Lett.* **122**, 257002, doi:10.1103/PhysRevLett.122.257002 (2019).

19   Wu, F., MacDonald, A. H. & Martin, I. Theory of Phonon-Mediated Superconductivity in Twisted Bilayer Graphene. *Phys. Rev. Lett.* **121**, 257001, doi:10.1103/PhysRevLett.121.257001 (2018).

20   Peltonen, T. J., Ojajärvi, R. & Heikkilä, T. T. Mean-field theory for superconductivity in twisted bilayer graphene. *Phys. Rev. B* **98**, doi:10.1103/PhysRevB.98.220504 (2018).

21   Liu, C. C., Zhang, L. D., Chen, W. Q. & Yang, F. Chiral Spin Density Wave and d+id Superconductivity in the Magic-Angle-Twisted Bilayer Graphene. *Phys. Rev. Lett.* **121**, 217001, doi:10.1103/PhysRevLett.121.217001 (2018).

22   Khalaf, E., Chatterjee, S., Bultinck, N., Zaletel, M. P. & Vishwanath, A. Charged skyrmions and topological origin of superconductivity in magic-angle graphene. *Sci. Adv.* **7**, eabf5299 (2021).

23   Sobota, J. A., He, Y. & Shen, Z.-X. Angle-resolved photoemission studies of quantum materials. *Rev. Mod. Phys.* **93**, doi:10.1103/RevModPhys.93.025006 (2021).

24   Yang, H. *et al.* Visualizing electronic structures of quantum materials by angle-resolved photoemission spectroscopy. *Nat. Rev. Mater.* **3**, 341-353, doi:10.1038/s41578-018-0047-2 (2018).

25   Uri, A. *et al.* Mapping the twist-angle disorder and Landau levels in magic-angle graphene. *Nature* **581**, 47-+, doi:10.1038/s41586-020-2255-3 (2020).

26   Koch, R. J. *et al.* Nano focusing of soft X-rays by a new capillary mirror optic. *Synchrotron Radiation News* **31**, 50-52, doi:10.1080/08940886.2018.1483660 (2018).

27   Lisi, S. *et al.* Observation of flat bands in twisted bilayer graphene. *Nat. Phys.* **17**, 189-193, doi:10.1038/s41567-020-01041-x (2021).

28   Utama, M. I. B. *et al.* Visualization of the flat electronic band in twisted bilayer graphene near the magic angle twist. *Nat. Phys.* **17**, 184-188, doi:10.1038/s41567-020-0974-x (2021).

29   Lee, J. J. *et al.* Interfacial mode coupling as the origin of the enhancement of T_c in FeSe films on $SrTiO_3$. *Nature* **515**, 245-248, doi:10.1038/nature13894 (2014).

30   Wang, Z. *et al.* Tailoring the nature and strength of electron-phonon interactions in the $SrTiO_3$ (001) 2D electron liquid. *Nat. Mater.* **15**, 835-839, doi:10.1038/nmat4623 (2016).

31   Chen, C. *et al.* Emergence of Interfacial Polarons from Electron-Phonon Coupling in Graphene/h-BN van der Waals Heterostructures. *Nano Lett.* **18**, 1082-1087, doi:10.1021/acs.nanolett.7b04604 (2018).

32   Liu, C., Chen, Y., Yazdani A., Bernevig, B. A., Electron-K Phonon Interaction In Twisted Bilayer Graphene, submitted.

33   Saito, Y., Ge, J., Watanabe, K., Taniguchi, T. & Young, A. F. Independent superconductors and correlated insulators in twisted bilayer graphene. *Nat. Phys.* **16**, 926-930, doi:10.1038/s41567-020-0928-3 (2020).

34   Song, Q. *et al.* Evidence of cooperative effect on the enhanced superconducting transition temperature at the FeSe/SrTiO$_3$ interface. *Nat. Commun.* **10**, 758, doi:10.1038/s41467-019-08560-z (2019).

35   Zhang, C. *et al.* Ubiquitous strong electron-phonon coupling at the interface of FeSe/SrTiO$_3$. *Nat. Commun.* **8**, 14468, doi:10.1038/ncomms14468 (2017).

36   Martnez, G. & Horsch, P. Spin polarons in the t-J model. *Phys. Rev. B Condens Matter* **44**, 317-331, doi:10.1103/physrevb.44.317 (1991).

37   Bostwick, A. *et al.* Observation of plasmarons in quasi-freestanding doped graphene. *Science* **328**, 999-1002, doi:10.1126/science.1186489 (2010).

38   Zhang, H. *et al.* Experimental evidence of plasmarons and effective fine structure constant in electron-doped graphene/h-BN heterostructure. *npj Quantum Mater.* **6**, doi:10.1038/s41535-021-00386-7 (2021).

39   Angeli, M., Tosatti, E. & Fabrizio, M. Valley Jahn-Teller Effect in Twisted Bilayer Graphene. *Phys. Rev. X* **9**, doi:10.1103/PhysRevX.9.041010 (2019).

40   Angeli, M. & Fabrizio, M. Jahn-Teller coupling to moire phonons in the continuum model formalism for small-angle twisted bilayer graphene. *Eur. Phys. J. Plus* **135**, 630, doi:10.1140/epjp/s13360-020-00647-7 (2020).

41   Yu, J. et al. Euler Obstructed Cooper Pairing in Twisted Bilayer Graphene: Nematic Nodal Superconductivity and Bounded Superfluid Weight. *arXiv preprint* arXiv:2202.02353 (2022).

42   Lanzara, A. *et al.* Evidence for ubiquitous strong electron-phonon coupling in high-temperature superconductors. *Nature* **412**, 510-514, doi:10.1038/35087518 (2001).

43   Reznik, D. *et al.* Electron-phonon coupling reflecting dynamic charge inhomogeneity in copper oxide superconductors. *Nature* **440**, 1170-1173, doi:10.1038/nature04704 (2006).

44   He, Y. *et al.* Rapid change of superconductivity and electron-phonon coupling through critical doping in Bi-2212. *Science* **362**, 62-+, doi:10.1126/science.aar3394 (2018).

45   Xiao, G., Cieplak, M. Z., Xiao, J. Q. & Chien, C. L. Magnetic pair-breaking effects: Moment formation and critical doping level in superconductingLa1.85Sr0.15Cu1−xAxO4systems (A=Fe,Co,Ni,Zn,Ga,Al). *Phys. Rev. B* **42**, 8752-8755, doi:10.1103/PhysRevB.42.8752 (1990).

46   Nachumi, B., et al. Muon Spin Relaxation Studies of Zn-Substitution Effects in High-Tc Cuprate Superconductors. *Phys. Rev. Lett.* **77**, 5421 (1996).

47   Fukuzumi, Y., Mizuhashi, K., Takenaka, K., & Uchida, S. Universal Superconductor-Insulator Transition and Tc Depression in Zn-Substituted High-T$_c$ Cuprates in the Underdoped Regime. *Phys. Rev. Lett.* **76**, 4 (1996).

48   Park, J. M., Cao, Y., Watanabe, K., Taniguchi, T. & Jarillo-Herrero, P. Tunable strongly coupled superconductivity in magic-angle twisted trilayer graphene. *Nature* **590**, 249-255 doi:10.1038/s41586-021-03192-0 (2021).

49   Polshyn, H. *et al.* Electrical switching of magnetic order in an orbital Chern insulator. *Nature* **588**, 66-+, doi:10.1038/s41586-020-2963-8 (2020).

50   Kim, K. *et al.* van der Waals Heterostructures with High Accuracy Rotational Alignment. *Nano Lett.* **16**, 1989-1995, doi:10.1021/acs.nanolett.5b05263 (2016).

51   Miao, W., Li, C., Han, X., Pan, D. & Dai, X. Truncated Atomic Plane Wave Method for the Subband Structure Calculations of Moire systems. *arXiv preprint* arXiv:2210.02026 (2022).
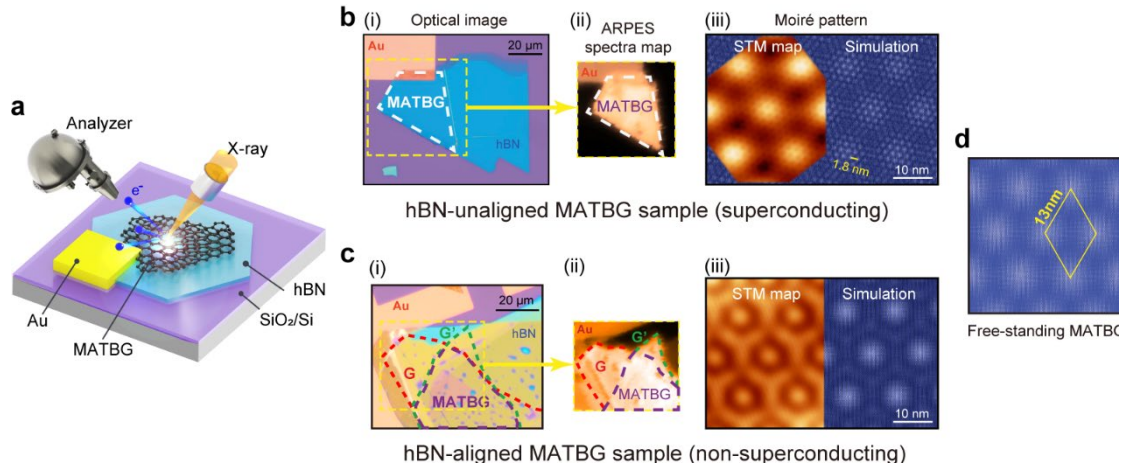
Acknowledgement

Fig. 1| μ-ARPES measurement and MATBG device geometries. (a), Schematic diagram of the μ-ARPES measurement geometry. **(b)**, Basic characterization of the MATBG (twist angle 1.06°) sample unaligned to its hBN substrate (8° rotational misalignment). (i) Optical image, with the substrate hBN, MATBG region (marked by white dashed lines) and the Au contact labelled. (ii) ARPES spectral intensity map covering the area enclosed by yellow dashed lines in (i) that highlights the MATBG region of the device. The spectral intensity is integrated within a binding energy of 0.2 eV, visualizing only conductive graphene and Au regions while omitting the hBN and SiO$_2$ regions. (iii) STM topographic image (V_b = −80 mV, I = 300 pA) and a simulation of the hBN-unaligned MATBG lattice, showing two sets of moiré patterns with different periodicity: the larger one (~13.3 nm) from the graphene/graphene moiré and the smaller one (~1.76 nm, marked by the yellow bar) from the graphene/hBN moiré, respectively. **(c)**, Same as (**b**) for the MATBG (1.08°) sample aligned with its hBN substrate (0.5° ± 0.1° rotational misalignment). (i) Optical image with monolayer graphene regions (G and G'; marked by red and green dashed lines) and the MATBG region (marked by purple dashed lines) labeled. The orange-colored regions of the hBN are the result of two overlapped hBN flakes used to encapsulate this sample's graphite back gate. (ii) ARPES spectral intensity map showing both monolayer graphene and MATBG regions corresponding to regions labelled in (i). (iii) STM topographic image (V_b = −300 mV, I = 100 pA) and lattice simulation, showing a commensurate moiré structure from MATBG and graphene/hBN as both have periodicity around 13 nm. **(d)**, Lattice simulation of free-standing MATBG (1.08°), demonstrating a moiré periodicity of ~13 nm.
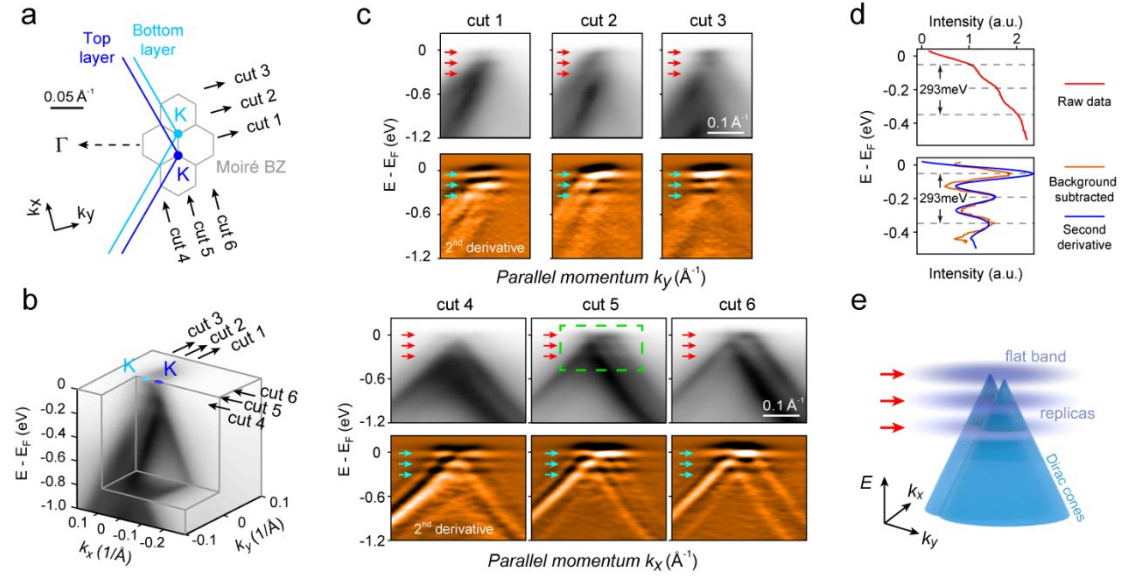
Fig. 2| Flat band replicas in hBN-unaligned MATBG sample. (a), Illustration of the MATBG moiré Brillouin zones (BZs) around the K point of top and bottom monolayer graphene BZs. Grey lines show the moiré BZs of MATBG. 'cut1'~ 'cut6' mark the coordinates of ARPES spectra in (c). **(b),** 3D intensity plot of ARPES spectra in the vicinity of the graphene K point, presenting an overview of the band structure of MATBG. **(c),** ARPES dispersion plots (top rows, marked by 'cut1'~ 'cut6' in (a-b)) and their associated 2nd derivative plots (bottom rows). Red / cyan arrows in top / bottom rows highlight the flat band and its first and second replicas. **(d),** Top panel: Integrated ARPES spectra intensity in the green dashed line box in (c). Bottom panel: The red curve represents the same data shown in the top panel with the removal of a smooth background (4th-degree polynomial). The blue curve represents the integrated intensity of the 2nd derivative plot within the same green dashed line box. Both red and blue curves show an energy spacing between the flat band and replicas of 150 ± 15 meV. (More details and analysis for other spectra can be found in Section II of SI) **(e),** Schematic diagram showing two Dirac dispersions from the individual graphene layers of MATBG and the system's associated flat band and replica flat bands. All ARPES spectra were taken with a photon energy of 95 eV at room temperature.
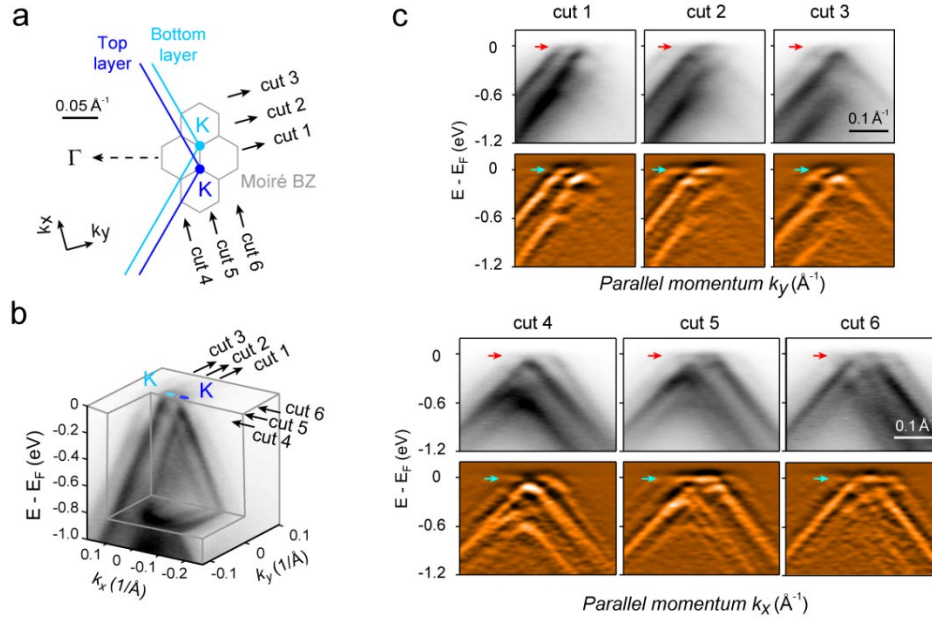
Fig. 3| Absence of flat band replicas in hBN-aligned MATBG sample. (a), Illustration of the MATBG moiré BZs around the K point of top and bottom monolayer graphene. Grey lines show the moiré BZs of MATBG. 'cut1' ~ 'cut6' mark the coordinates of ARPES spectra in (c). **(b),** 3D intensity plot of ARPES spectra in the vicinity of the graphene K point, presenting an overview of the band structure of hBN-aligned MATBG sample. Here, the electronic structure of MATBG is modified by the commensurate alignment of hBN as compared to the unaligned case illustrated in Fig. 2. **(c),** ARPES dispersion plots and 2nd derivative plots taken along the same momentum directions (marked in (a-b)) as those in Fig. 2 for the hBN-unaligned MATBG sample. The flat band is labelled by red / cyan arrows. No signs of replicas of the flat band were observed, in contrast to the data shown in Fig. 2.
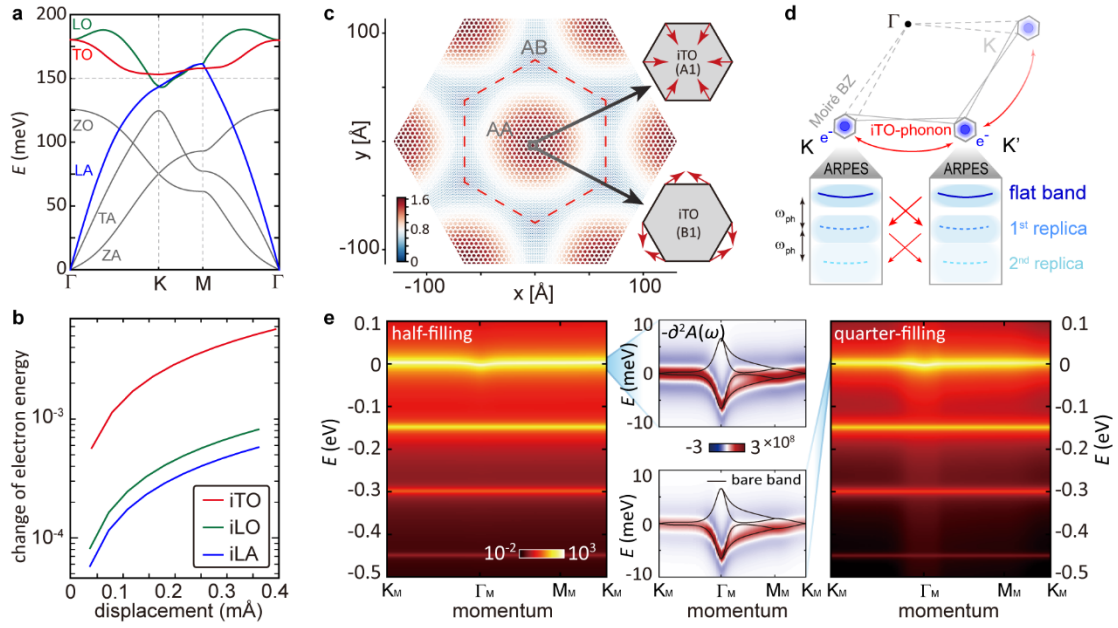
Fig. 4| Inter-valley electron-phonon coupling in MATBG. (a), Calculated phonon spectra of single-layer graphene. Three phonon modes (LO (longitudinal optical mode), TO (transverse optical mode), LA (longitudinal acoustic mode)) with ~150 meV energy around the K point are highlighted. **(b),** Calculated effective electron-phonon coupling (EPC) strength of iTO (in-plane TO), iLO and iTA phonon modes as a function of average lattice distortion. The EPC strength of iTO mode is almost an order of magnitude larger than the other two modes. (More details can be found in SI, Section IV, V.). **(c),** Real-space lattice distortion magnitude induced by iTO phonons, which peaks at the AA-stacking regions and diminishes at the AB-stacking regions. Atomic displacement directions around AA-stacking regions for A_1 and B_1 iTO modes are illustrated on the inset. The broken red hexagon marks the Wigner-Seitz cell of the MATBG. **(d),** Schematic diagram of the intervalley EPC in MATBG. Flat-band electrons from two moiré BZs at the K and K' points are exchanged via the scattering of iTO phonons, which generates shake-off replica bands separated by energy intervals of the iTO phonon energy. **(e),** Simulated photoemission spectra of the flat band and replicas at half- and quarter-filling of the flat band electrons, respectively. The middle panel shows the zoomed-in second-derivative spectra of the flat bands, where the solid lines are the calculated dispersion of bare bands without EPC (More details can be found in Section VI of SI).